

Unprotected quadratic band crossing points and quantum anomalous Hall effect in FeB₂ monolayer

Dongyu Wu,^{1, 2, *} Yunpeng Huang,^{1, *} Song Sun,^{1, 2} Jiacheng Gao,^{1, 2} Zhaopeng Guo,^{1, †} Hongming Weng,^{1, 2} Zhong Fang,^{1, 2} Kun Jiang,¹ and Zhijun Wang^{1, 2, ‡}

¹*Beijing National Laboratory for Condensed Matter Physics,
and Institute of Physics, Chinese Academy of Sciences, Beijing 100190, China*

²*University of Chinese Academy of Sciences, Beijing 100049, China*

(Dated: March 1, 2022)

Quadratic band crossing points (QBCPs) and quantum anomalous Hall effect (QAHE) have attracted attentions of both theoretical and experimental researchers in recent years. Based on first principles calculations, we find that FeB₂ monolayer is a nonmagnetic semimetal with QBCPs at K . Through symmetry analysis and $\mathbf{k} \cdot \mathbf{p}$ invariant theory, we explain the origin of QBCPs and the associated Berry phase of 2π . Once introducing interactions, we find that there is a spontaneous-time-reversal-breaking instability of the spinful QBCPs, which gives rise to a $C = 2$ QAH insulator with orbital moment ordering.

I. INTRODUCTION

In a two-dimensional (2D) system, the finite density of states associated with the parabolic dispersion could lead instability for arbitrarily weak interactions [1–5]. For a quadratic band crossing point (QBCP) to be stable without fine-tuning, the system must be time-reversal invariant and the QBCP must have C_4 or C_6 rotational symmetry [1]. The interaction would lead to the possibility of spontaneous breaking of rotational symmetry (nematic phase) or time-reversal invariance. However, the QBCPs at the threefold-invariant momentum on the honeycomb lattice and relatives can be unprotected. The introduction of interactions leads to qualitatively different low-energy behavior, even without the breaking of the underlying symmetries [2]. Although there are many theoretical studies of spinless QBCPs on many tailored 2D systems, such as single layer graphene [2, 3] and Bernal-stacked bilayer graphene [4], the unprotected QBCPs have not been reported in any spinful system and its possible instabilities have not been discussed yet.

Besides, topological states, including quantum anomalous Hall (QAH) state, have attracted considerable research interest recently [6–13]. In spite of plenty of material proposals for QAH state [14–19], the observation of the QAH effect is still full of challenges and has been merely realized in few systems such as, Cr-doped and V-doped (Bi,Sb)₂Te₃ thin films [20, 21], magnetic topological insulator MnBi₂Te₄ [22] and twisted bilayer graphene (TBG) [23]. Previous theoretical studies also show that the QAH effect can be realized in graphene by introducing both exchange field and Rashba spin-orbit coupling (SOC) due to its unique linear Dirac band dispersions [15].

In recent years, MB_2 (M = transition metal) monolayers are predicted to be 2D Dirac cone materials theoretically in the absence of SOC, such as TiB₂ [24], FeB₂ [25] and HfB₂ [26] monolayers. Unlike graphene, these Dirac bands of FeB₂ originate from d states of the transition metal Fe, which has substantial Rashba SOC effect and is very likely coupled to magnetic field. A Chern insulator can be achieved once it is grown on an insulating magnetic substrate. In this article, we find that FeB₂ monolayer is a nonmagnetic semimetal with QBCPs based on first-principle calculations. Without including SOC, there is a linearly dispersive Dirac node at K (resp. K') with a Berry phase π (resp. $-\pi$), protected by the combined symmetry of time reversal and twofold rotation (*i.e.*, TC_{2z}). Once including SOC, the Dirac node becomes a QBCP and its Berry phase becomes 2π (-2π) at K (K'), which were previously considered as linear band crossing points [37]. These characters can be captured by the $\mathbf{k} \cdot \mathbf{p}$ effective Hamiltonians. With an insulating magnetic substrate, FeB₂ monolayer is turned to be a Chern insulator with two chiral edge states, which is stimulated by the fixed-moment calculations. More interestingly, once we introduce the interactions, an instability towards a $C = 2$ QAH state is found, which is formed by the orbital moment ordering.

II. CALCULATION METHOD

We performed the first-principles calculations within the framework of the density functional theory (DFT) using the projector augmented wave (PAW) method [27, 28], which is implemented in Vienna *ab initio* simulation package (VASP) [29, 30]. The Perdew-Burke-Ernzerhof (PBE) generalized gradient approximation exchange-correlations functional [31] was implemented in calculations. The cut-off energy for plane wave expansion was 945 eV, and $12 \times 12 \times 1$ k -point sampling grids were used in the self-consistent process. A vacuum layer of 20 Å was chosen to avoid interaction between neighboring layers.

* These authors contributed equally to this work.

† zpguo@iphy.ac.cn

‡ wzj@iphy.ac.cn

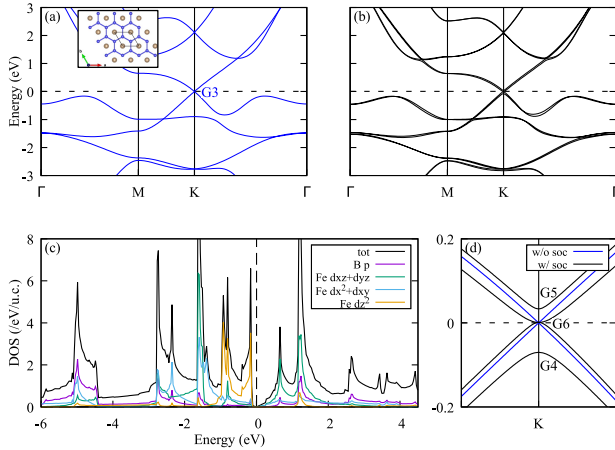


FIG. 1. (color online). The calculated electronic structures of FeB_2 monolayer without (a) and with (b) SOC. The inset in (a) shows the crystal structure of FeB_2 monolayer, where Fe and B atoms are marked by brown and blue balls. The irrep of two-fold bands at K is denoted by G_3 . (c) The total DOS and projected DOS of B- p and Fe- d orbitals, respectively. (d) The zoom-in plot of band structures near K point. The irreps of four low-energy SOC bands at K are denoted by G_4 , G_5 and G_6 .

SOC was taken into account within the second variational method self-consistently. The irreducible representations (irreps) were obtained by the program IRVSP [32]. The maximally localized Wannier functions (MLWFs) were constructed by Fe-3d, B-2s and B-2p orbitals using Wannier90 package [33]. The edge states were calculated using surface Green's function of the semi-infinite system based on the iterative scheme [34–36].

III. DFT RESULTS

The crystal structure of FeB_2 monolayer belongs to space group $P6mm$ (No. 183), as shown in Fig. 1(a). One unit cell contains two B atoms and one Fe atom, which are located at $2b$ and $1a$ Wyckoff positions, respectively. B atoms are arranged in a honeycomb lattice, and Fe atoms are located in the middle of the hexagons. The PBE band structure of FeB_2 monolayer is shown in Fig. 1(a), there is a linearly dispersive Dirac point at K near the Fermi level (E_F). Therefore, FeB_2 monolayer was predicted to be a 2D Dirac semimetal [25, 37]. The little point group at K is C_{3v} , and the twofold Dirac bands belong to G_3 irreducible representation (irrep), which are consistent with Ref. [37]. The total and projected density of states (DOS) are plotted in Fig. 1(c). They show that the hybridization between Fe and B is strong, while the electronic states near E_F are mainly contributed by d_{z^2} and $d_{xz} + d_{yz}$ electrons of Fe atoms (the orbital-resolved band structures are given in Appendix A). Once including SOC, as shown in Figs. 1(b,d), the two Dirac bands split into two non-degenerate bands

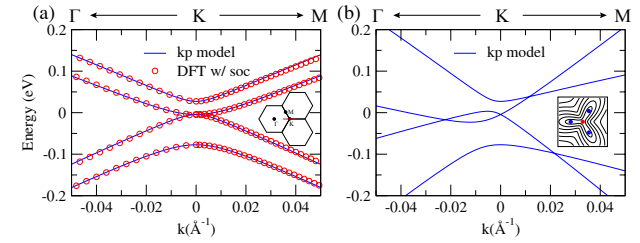


FIG. 2. (color online). (a) The band dispersions (blue lines) of the four-band effective Hamiltonian in Eq. (2) with the parameters in Table I agree well with the bands (red circles) from the DFT calculation. The k -path is indicated by the red line in the inset of the Brillouin zone. (b) The band dispersions of the effective model with $C_1 = -3.03 \text{ eV}\text{\AA}$ and $C_2 = -3.03 \text{ eV}\text{\AA}^2$ are plotted for comparison. The inset shows iso-energy-gap lines in the vicinity of K point. The Dirac points with Berry phases π and $-\pi$ are colored in blue and red, respectively.

(G_4 and G_5) and one doubly-degenerate band (G_6) at K , exhibiting quadratic band dispersion, which were mistakenly considered to be linear dispersion.

IV. LOW-ENERGY EFFECTIVE MODELS

Based on the theory of invariants, we derive the low-energy effective Hamiltonian $H_K(\vec{k})$ (*i.e.*, \vec{k} is the offset momentum from K). Under the basis of G_3 irrep, *e.g.* $\{|d_{xz} + id_{yz}\rangle, |d_{xz} - id_{yz}\rangle\}$, it reads,

$$H_K(\vec{k}) = \begin{pmatrix} M_1(\vec{k}) & Ak_+ \\ Ak_- & M_1(\vec{k}) \end{pmatrix}. \quad (1)$$

After considering the spin degree of freedom, the four-band Hamiltonian becomes (in the basis of $\{|\uparrow\rangle, |\downarrow\rangle\} \otimes \{|d_{xz} + id_{yz}\rangle, |d_{xz} - id_{yz}\rangle\}$),

$$H_K^{so}(\vec{k}) = \sigma_0 \otimes H_K(\vec{k}) + \begin{pmatrix} M_2(\vec{k}) & & & \\ 0 & -M_2(\vec{k}) & & \\ iBk_+ & iC(\vec{k}) & -M_2(\vec{k}) & \\ iM_3(\vec{k}) & iBk_+ & 0 & M_2(\vec{k}) \end{pmatrix}^\dagger, \quad (2)$$

where $k_\pm = k_x \pm ik_y$, $C(\vec{k}) = C_1k_- + C_2k_+^2$, $M_{\alpha=1,2,3}(\vec{k}) = E_\alpha + F_\alpha k_\perp^2$ with $k_\perp^2 = k_x^2 + k_y^2$, and σ_0 is the identity matrix in the spin space. We derive the k^2 terms in this Hamiltonian, since they are crucial to get quadratic band dispersion in the following effective 2×2 Hamiltonian.

By fitting the DFT band structure in the vicinity of K , the parameters are obtained in Table I and the results are shown in Fig. 2(a). The $\mathbf{k} \cdot \mathbf{p}$ model reproduces the QBCP at K , and the Berry phase for the QBCP is 2π . The 2nd and 3rd bases form G_6 irrep of C_{3v} double group, *i.e.*, $\{|d_{xz} - id_{yz}, \uparrow\rangle, |d_{xz} + id_{yz}, \downarrow\rangle\}$. To evaluate

the positions of Dirac points, a simplest model under G_6 irrep can be obtained as below,

$$H'_K(\vec{k}) = \begin{pmatrix} M_1(\vec{k}) - M_2(\vec{k}) & -iC'_1 k_+ - iC'_2 k_-^2 \\ iC'_1 k_- + iC'_2 k_+^2 & M_1(\vec{k}) - M_2(\vec{k}) \end{pmatrix}, \quad (3)$$

where C'_1 and C'_2 are modified parameters after down-folding. Its two eigenvalues are solved as $E_{\pm} = M_1(\vec{k}) - M_2(\vec{k}) \pm \sqrt{\Delta(\vec{k})}$ with

$$\Delta(\vec{k}) = C'_2 k_{\perp}^4 + 2C'_1 C'_2 k_x (k_x^2 - 3k_y^2) + C'_1^2 k_{\perp}^2. \quad (4)$$

The gapless points satisfy the condition of $\Delta(\vec{k}) = 0$. Assuming $k_y = 0$, the equation is simplified to $C'_2 k_x^4 + 2C'_1 C'_2 k_x^3 + C'_1^2 k_x^2 = 0$, giving rise to two Dirac points located at $k_x = 0$ and $-C'_1/C'_2$. The detailed calculations show that the two Dirac points have opposite π Berry phase. The distance between them is $d_0 = |C'_1/C'_2|$ in momentum space. Considering C_{3z} symmetry, there must be two additional Dirac points around K , as shown in the inset of Fig. 2(b). No other gapless point is found (see the proof in Appendix B).

As the Dirac points and the quantized Berry phase of π are protected by the antiunitary symmetry TC_{2z} , the above discussion should be valid for the four-band model $H_K^{so}(\vec{k})$ as well. In the band dispersions of Fig. 2(a), we numerically get $d_0 \sim 5.2 \times 10^{-5} \text{ \AA}^{-1}$. The ratio $d_0/d_{\Gamma K}$ is 0.004% ($d_{\Gamma K} = 1.321 \text{ \AA}^{-1}$), which is too small to identify in FeB₂ monolayer. Therefore, it's rational to consider the K point is a double Dirac point with quadratic band dispersions in FeB₂ monolayer, corresponding to a 2π Berry phase, even though the quadratic band dispersion is not protected by rotational symmetry. Note that it's similar to the case in the magic-angle TBG, where the velocity of K becomes zero [38, 39]. For comparison, we plot the band dispersions of the four-band model with modified C_1 and C_2 parameters in Fig. 2(b), from which d_0 is read to be 0.223 \AA^{-1} ($\sim 0.17 d_{\Gamma K}$). The iso-energy-gap contours are shown in the vicinity of K points in its inset. A Dirac point ($-\pi$) at K and three other Dirac points (π) are clearly shown.

Thus, a Chern insulator can be achieved in FeB₂ monolayer with an external magnetic field (e.g. grown on an insulating magnetic substrate). As shown in Figs. 3(a,b), with inplane external magnetic field keeping TC_{2z} , the double Dirac point at K splits into two Dirac points. When the magnetism is out-of-plane, the FeB₂ becomes a Chern insulator with two chiral edge states in Fig. 3(c).

TABLE I. The parameters in the effective $\mathbf{k} \cdot \mathbf{p}$ Hamiltonian.

0th order	eV	1st order	eV·Å	2nd order	eV·Å ²
E_1	-0.0147	A	2.6021	F_1	-1.7201
E_2	-0.0103	B	0.0141	F_2	0.2346
E_3	0.0522	C_1	-0.0080	F_3	0.5754
				C_2	-0.1010

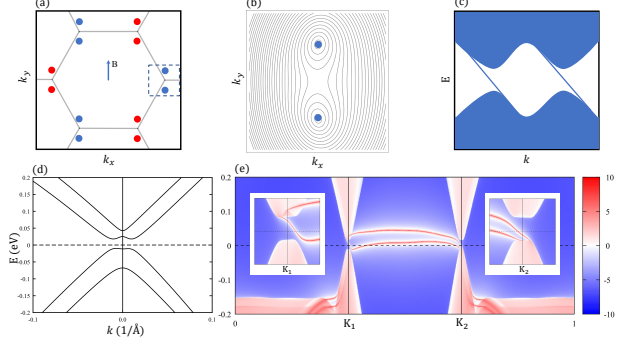


FIG. 3. (color online). The electronic structure of FeB₂ monolayer in magnetic field. (a) The distribution of Dirac points with inplane magnetic field (which keeps TC_{2z}). The arrow marks the direction of the magnetic field. Each QBCP splits into two Dirac points with identical π Berry phase. (b) The iso-energy-gap contours are plotted in the dashed rectangle area in (a). (c) The schematic diagram of two chiral edge states of FeB₂ monolayer with z -directed magnetic field. (d) The computed band structure of FeB₂ monolayer with a fixed magnetic moment $0.01 \mu_B$ on the Fe atom. (e) The B-terminated zigzag-edge state of fixed magnetic moment FeB₂ monolayer. The inserts show the zoom-in plots around $K_{1,2}$. The K_1 and K_2 are the projections of K and K' on the edge.

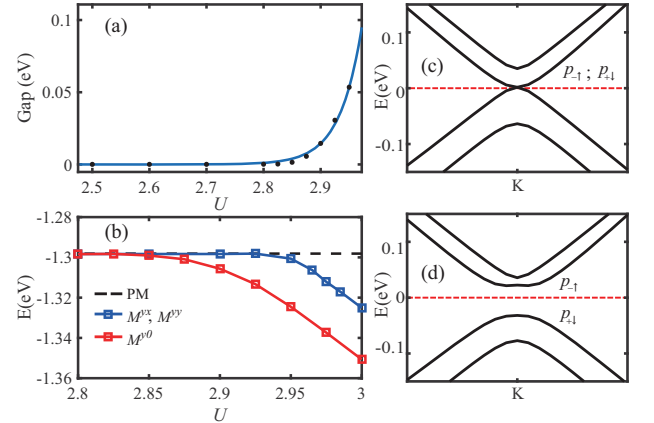


FIG. 4. (a) The energy gap behavior when varying the Coulomb interaction strength U , the solid blue line is fitting to the data by exponential function $\Delta = a * \exp(-1/(b * U))$ with $a = 3.812 \times 10^{30}$ and $b = 4.622 \times 10^{-3}$. (b) The energy of the obtained states in the self-consistency calculation as a function of the interaction strength U . (c-d) The quasi-particle energy bands when $U = 0$ and $U = 2.95 \text{ eV}$, the orbital contributions of QBCP are also shown. The basis $P_{\pm\alpha} = \frac{1}{\sqrt{2}}(d_{xz,\alpha} \pm i d_{yz,\alpha})$, $\alpha = \uparrow, \downarrow$. We fixed $U = U'$ in the calculation of all figures.

The Zeeman's coupling Hamiltonian is given in Appendix C. To simulate the spin-polarized state of FeB₂ induced by the out-of-plane magnetism of substrates, we have performed the DFT calculations with a fixed moment (e.g. $0.01 \mu_B$ on Fe atom) in the z direction. Its spin-polarized band structure is obtained in Fig. 3(d).

The FeB_2 monolayer becomes a Chern insulator, which is compatible with the result of graphene with both Rashba SOC and an exchange field [15]. Then, we construct the maximally localized Wannier functions (MLWFs) and calculate the edge spectra, as shown in Fig. 3(e). Two chiral edge states connecting the conduction continuum and valence continuum indicate a Chern number of 2.

V. ORBITAL-MOMENT-INDUCED QAH WITH INTERACTIONS

Interestingly, once considering the onsite Coulomb interaction, we find the instability towards a gapped phase with orbital moment ordering, and the system exhibiting a QAH effect. Using d_{xz} , d_{yz} and d_{z^2} orbitals of Fe atoms, a spinful three-orbital tight-binding model is constructed to capture the DFT band structure (see more details in Appendix D). The Coulomb interaction considered in d_{xz} and d_{yz} orbitals is written as,

$$H_{int} = U \sum_l n_{l,\uparrow} n_{l,\downarrow} + U' \sum_{l < l', \alpha, \beta} n_{l,\alpha} n_{l',\beta}, \quad (5)$$

where $n_{l,\alpha}$ represents the electron density on orbital l with spin α and $\alpha, \beta = \uparrow, \downarrow$. We further employ the Hartree-Fock approximation to treat the Coulomb interaction. And the order parameters are defined as

$$M^{\mu\nu} = \sum_{l, l'} \sum_{\alpha, \beta} \tau_{l, l'}^{\mu} \sigma_{\alpha, \beta}^{\nu} \langle d_{l, \alpha}^{\dagger} d_{l', \beta} \rangle. \quad (6)$$

Here, the $d_{l, \alpha}^{\dagger}$ operator creates (annihilates) an electron in orbital l with spin α , τ^{μ} and σ^{ν} ($\mu, \nu = 0, x, y, z$) are the identity with three Pauli matrices representing the orbital and spin degree of freedom respectively. We self-consistently investigate the zero-temperature phase diagram, and the results are shown in the Fig. 4.

In the self-consistency calculations, we exclude the channels for SOC relevant order parameter M^{yz} and the

symmetric part of the electron density terms M^{00} , which have already been considered in the DFT calculation. The Coulomb interactions between d_{xz} and d_{yz} orbitals intrinsically stimulate the orbital-magnetization phases respectively with order parameters M^{yx} , M^{yy} and M^{y0} . All three orderings break the TC_{2z} symmetry and open the gap at the K point. The M^{yx} phase and M^{yy} phase are related by C_6 symmetry, while the M^{y0} phase is the ground state in the presence of SOC. The gap width exponentially grows when increasing the Coulomb interaction strength U . The gapped system then becomes a Chern insulator with $C = 2$.

VI. CONCLUSION

In conclusion, we have explored the electronic structures and topological property of FeB_2 monolayer. Without SOC, FeB_2 monolayer has linear band crossing points at K points. Upon including SOC, they become QBCPs with the Berry phase of 2π . Based on $\mathbf{k} \cdot \mathbf{p}$ effective Hamiltonians, we demonstrate that the QBCPs are not protected by rotational symmetry. There are actually one Dirac point at K and three C_3 -related Dirac points with opposite π Berry phase around it. The appearance of QBCPs (or zero velocity at K) is similar to the case in the magic-angle TBG. FeB_2 monolayer is a good platform for the study the instability of QBCPs. Most importantly, with Coulomb interactions, FeB_2 monolayer turns out to be a $C = 2$ QAH insulator because of the orbital-moment-ordering instability in spinful QBCPs.

ACKNOWLEDGMENTS

This work was supported by the National Natural Science Foundation of China (Grants No. 11974395, U2032204), the Strategic Priority Research Program of Chinese Academy of Sciences (Grant No. XDB33000000), and the Center for Materials Genome.

[1] K. Sun, H. Yao, E. Fradkin, and S. A. Kivelson, *Phys. Rev. Lett.* **103**, 046811 (2009).
[2] S. Hesselmann, C. Honerkamp, S. Wessel, and T. C. Lang, *Phys. Rev. B* **101**, 075128 (2020).
[3] G. Montambaux, *The European Physical Journal B* **85**, 375 (2012).
[4] O. Vafek and K. Yang, *Phys. Rev. B* **81**, 041401 (2010).
[5] Q.-F. Liang, J. Zhou, R. Yu, X. Wang, and H. Weng, *Phys. Rev. B* **96**, 205412.
[6] D. J. Thouless, M. Kohmoto, M. P. Nightingale, and M. Den尼js, *Phys. Rev. Lett.* **49**, 405 (1982).
[7] B. A. Bernevig, T. L. Hughes, and S.-C. Zhang, *Science* **314**, 1757 (2006).
[8] H. Zhang, C.-X. Liu, X.-L. Qi, X. Dai, Z. Fang, and S.-C. Zhang, *Nat. Phys.* **5**, 438 (2009).
[9] S. Nie, L. Xing, R. Jin, W. Xie, Z. Wang, and F. B. Prinz, *Phys. Rev. B* **98**, 125143 (2018).
[10] X. Wan, A. M. Turner, A. Vishwanath, and S. Y. Savrasov, *Phys. Rev. B* **83**, 205101 (2011).
[11] H. Weng, C. Fang, Z. Fang, B. A. Bernevig, and X. Dai, *Phys. Rev. X* **5**, 011029 (2015).
[12] S.-Y. Xu, I. Belopolski, N. Alidoust, M. Neupane, G. Bian, C. Zhang, R. Sankar, G. Chang, Z. Yuan, C.-C. Lee, S.-M. Huang, H. Zheng, J. Ma, D. S. Sanchez, B. Wang, A. Bansil, F. Chou, P. P. Shibayev, H. Lin, S. Jia, and M. Z. Hasan, *Science* **349**, 613 (2015).
[13] Z. Wang, M. G. Vergniory, S. Kushwaha, M. Hirschberger, E. V. Chulkov, A. Ernst, N. P. Ong, R. J. Cava, and B. A. Bernevig, *Phys. Rev. Lett.* **117**, 236401 (2016).

- [14] R. Yu, W. Zhang, H.-J. Zhang, S.-C. Zhang, X. Dai, and Z. Fang, *Science* **329**, 61 (2010).
- [15] Z. Qiao, S. A. Yang, W. Feng, W.-K. Tse, J. Ding, Y. Yao, J. Wang, and Q. Niu, *Phys. Rev. B* **82**, 161414 (2010).
- [16] K. F. Garrity and D. Vanderbilt, *Phys. Rev. Lett.* **110**, 116802 (2013).
- [17] Y. Xue, J. Y. Zhang, B. Zhao, X. Y. Wei, and Z. Q. Yang, *Nanoscale* **10**, 8569 (2018).
- [18] Z. F. Wang, Z. Liu, and F. Liu, *Phys. Rev. Lett.* **110**, 196801 (2013).
- [19] S. Nie, Y. Sun, F. B. Prinz, Z. Wang, H. Weng, Z. Fang, and X. Dai, *Phys. Rev. Lett.* **124**, 076403 (2020).
- [20] C.-Z. Chang, J. Zhang, X. Feng, J. Shen, Z. Zhang, M. Guo, K. Li, Y. Ou, P. Wei, L.-L. Wang, Z.-Q. Ji, Y. Feng, S. Ji, X. Chen, J. Jia, X. Dai, Z. Fang, S.-C. Zhang, K. He, Y. Wang, L. Lu, X.-C. Ma, and Q.-K. Xue, *Science* **340**, 167 (2013).
- [21] C.-Z. Chang, W. Zhao, D. Y. Kim, H. Zhang, B. A. Assaf, D. Heiman, S.-C. Zhang, C. Liu, M. H. W. Chan, and J. S. Moodera, *Nat. Mater.* **14**, 473 (2015).
- [22] Y. Deng, Y. Yu, M. Z. Shi, Z. Guo, Z. Xu, J. Wang, X. H. Chen, and Y. Zhang, *Science* **367**, 895 (2020).
- [23] M. Serlin, C. L. Tscherhart, H. Polshyn, Y. Zhang, J. Zhu, K. Watanabe, T. Taniguchi, L. Balents, and A. F. Young, *Science* **367**, 900 (2020).
- [24] L. Z. Zhang, Z. F. Wang, S. X. Du, H. J. Gao, and F. Liu, *Phys. Rev. B* **90**, 161402 (2014).
- [25] H. Zhang, Y. Li, J. Hou, A. Du, and Z. Chen, *Nano Lett.* **16**, 6124 (2016).
- [26] Z. Liu, P. Wang, Q. Cui, G. Yang, S. Jin, and K. Xiong, *Rsc Advances* **9**, 2740 (2019).
- [27] P. E. Blochl, *Phys. Rev. B* **50**, 17953 (1994).
- [28] G. Kresse and D. Joubert, *Phys. Rev. B* **59**, 1758 (1999).
- [29] G. Kresse and J. Furthmuller, *Comp. Mater. Sci.* **6**, 15 (1996).
- [30] G. Kresse and J. Furthmuller, *Phys. Rev. B* **54**, 11169 (1996).
- [31] J. P. Perdew, K. Burke, and M. Ernzerhof, *Phys. Rev. Lett.* **77**, 3865 (1996).
- [32] J. C. Gao, Q. S. Wu, C. Persson, and Z. J. Wang, *Comp. Phys. Commun.* **261**, 107760 (2021).
- [33] G. Pizzi, V. Vitale, R. Arita, S. Bluegel, F. Freimuth, G. Geranton, M. Gibertini, D. Gresch, C. Johnson, T. Koretsune, J. Ibanez-Azpiroz, H. Lee, J.-M. Lihm, D. Marchand, A. Marrazzo, Y. Mokrousov, J. I. Mustafa, Y. Nohara, Y. Nomura, L. Paulatto, S. Ponce, T. Ponweiser, J. Qiao, F. Thoelle, S. S. Tsirkin, M. Wierzbowska, N. Marzari, D. Vanderbilt, I. Souza, A. A. Mostofi, and J. R. Yates, *J. Phys.-Condens. Matter* **32**, 165902 (2020).
- [34] M. P. L. Sancho, J. M. L. Sancho, and J. Rubio, *J. Phys. F-Met. Phys.* **14**, 1205 (1984).
- [35] M. P. L. Sancho, J. M. L. Sancho, and J. Rubio, *J. Phys. F-Met. Phys.* **15**, 851 (1985).
- [36] Q. Wu, S. Zhang, H.-F. Song, M. Troyer, and A. A. Soluyanov, *Comp. Phys. Commun.* **224**, 405 (2018).
- [37] W. Luo, J. Ji, J. Lu, X. Zhang, and H. Xiang, *Phys. Rev. B* **101**, 195111 (2020).
- [38] R. Bistritzer and A. H. MacDonald, *Proc. Natl. Acad. Sci. USA* **108**, 12233 (2011).
- [39] Z. Song, Z. Wang, W. Shi, G. Li, C. Fang, and B. A. Bernevig, *Phys. Rev. Lett.* **123**, 036401 (2019).

APPENDIX

A. Orbital-resolved band structures

The orbital-resolved band structures are presented in Fig. S1. We found that the low-energy bands near E_F (*i.e.*, $-3\text{eV} < E - E_F < 1\text{eV}$) mainly comes from Fe-*d* orbitals.

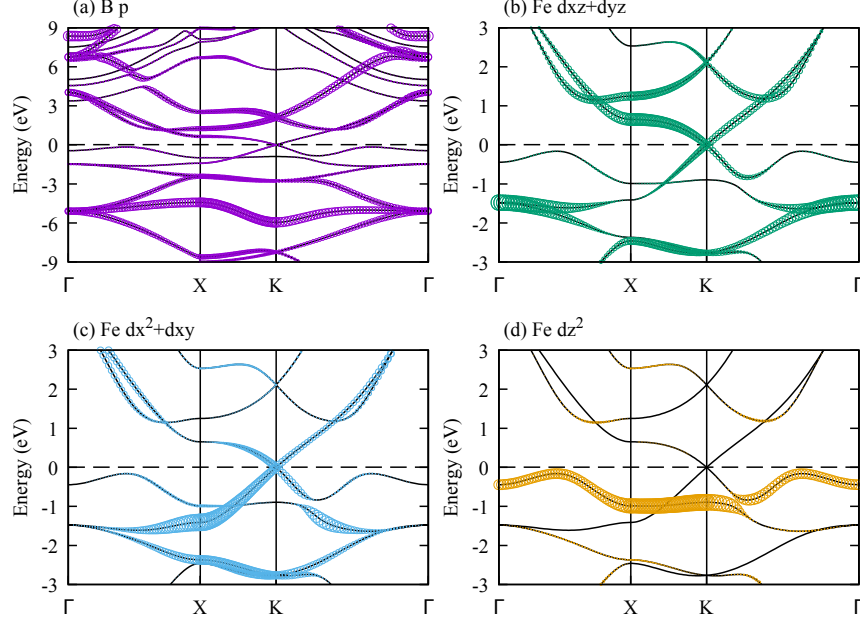


FIG. S1. (color online). The orbital-resolved band structures of monolayer FeB_2 of (a) p orbitals of B atoms, (b) $d_{xz} + d_{yz}$, (c) $d_{x^2-y^2} + d_{xy}$ and (d) d_{z^2} orbitals of Fe atoms.

B. Low-energy effective Hamiltonians

Without SOC, the band crossing at K belongs to two-dimensional irreducible representation (irrep) G_3 (labeled in the double point group of C_{3v}). When considering SOC, it changes into $G_4 \oplus G_5 \oplus G_6$ irreps. We choose the bases of $\{|\uparrow\rangle, |\downarrow\rangle\} \otimes \{|d_{xz} + id_{yz}\rangle, |d_{xz} - id_{yz}\rangle\}$ to construct the 4×4 Hamiltonian. The $\mathbf{k} \cdot \mathbf{p}$ Hamiltonian around K is constrained by the double point group C_{3v} and an anti-unitary symmetry TC_{2z} . Under these bases, the generators (*e.g.* C_{3z} , M_y , and $C_{6z}T$) are represented as follows,

$$C_{3z} = \begin{pmatrix} -1 & 0 & 0 & 0 \\ 0 & e^{i\pi/3} & 0 & 0 \\ 0 & 0 & e^{-i\pi/3} & 0 \\ 0 & 0 & 0 & -1 \end{pmatrix}, \quad (7)$$

$$M_y = \begin{pmatrix} 0 & 0 & 0 & 1 \\ 0 & 0 & 1 & 0 \\ 0 & -1 & 0 & 0 \\ -1 & 0 & 0 & 0 \end{pmatrix}, \quad (8)$$

$$C_{6z}T = \begin{pmatrix} 0 & 0 & 0 & i \\ 0 & 0 & -e^{i\pi/6} & 0 \\ 0 & e^{-i\pi/6} & 0 & 0 \\ i & 0 & 0 & 0 \end{pmatrix} \mathcal{K}, \quad (9)$$

where \mathcal{K} denotes the complex conjugation. Using the theory of invariants, we constructed the $\mathbf{k} \cdot \mathbf{p}$ effective Hamiltonian below,

$$H_K^{so}(\vec{k}) = \begin{pmatrix} M_1(\vec{k}) + M_2(\vec{k}) & & & \dagger \\ Ak_- & M_1(\vec{k}) - M_2(\vec{k}) & & \\ iBk_+ & iC(\vec{k}) & M_1(\vec{k}) - M_2(\vec{k}) & \\ iM_3(\vec{k}) & iBk_+ & Ak_- & M_1(\vec{k}) + M_2(\vec{k}) \end{pmatrix}, \quad (10)$$

where $k_{\pm} = k_x \pm ik_y$, $C(\vec{k}) = C_1k_- + C_2k_+^2$, and $M_{\alpha=1,2,3}(\vec{k}) = E_{\alpha} + F_{\alpha}k_{\perp}^2$ with $k_{\perp}^2 = k_x^2 + k_y^2$. On the other hand, the simplest two-band $\mathbf{k} \cdot \mathbf{p}$ Hamiltonian under the two bases of G_6 irrep is also derived as,

$$H'_K(\vec{k}) = \begin{pmatrix} M_1(\vec{k}) - M_2(\vec{k}) & -iC'_1k_+ - iC'_2k_- \\ iC'_1k_- + iC'_2k_+^2 & M_1(\vec{k}) - M_2(\vec{k}) \end{pmatrix}. \quad (11)$$

Then, we will prove there are only four Dirac points in the above two-band Hamiltonian. With the condition $k_x = ak_y$ ($a \neq 0$), we will get solutions $(k_x = (a^2(3 - a^2)C'_1/C'_2 \pm \sqrt{-(3a^3 - a^2)^2(C'_1/C'_2)^2})/(1 + a^2)^2, k_y = k_x/a)$. To get real roots of the solutions, $\sqrt{-(3a^3 - a^2)^2(C'_1/C'_2)^2}$ should be zero. If $C'_1/C'_2 \neq 0$ and $a \neq 0$, then $3a^2 - 1 = 0$, thus $a = \pm\sqrt{3}/3$. Taking $k_x = \pm k_y/\sqrt{3}$ into the equation, we can get the positions of two Dirac points, which are $(C'_1/2C'_2, \pm\sqrt{3}C'_1/2C'_2)$. Combining the results of conditions $k_x = 0, k_y = 0$ and $k_x = ak_y$ ($a \neq 0$), there are four Dirac points in two-band $\mathbf{k} \cdot \mathbf{p}$ Hamiltonian of G_6 irrep. One Dirac point is located at $(0, 0)$, and three C_3 -related Dirac points are located at $(-C'_1/C'_2, 0)$ and $(C'_1/2C'_2, \pm\sqrt{3}C'_1/2C'_2)$. These three Dirac points are connected by C_3 symmetry, and their distances from K are $d_0 = |C'_1/C'_2|$. Thus, with the $|C'_1/C'_2|$ decreases, the Dirac points will come close to the K point. If C'_1 decrease to zero, the eigenvalues of Eq. (11) are $E_{\pm} = M_1(\vec{k}) - M_2(\vec{k}) \pm |C'_2|(k_x^2 + k_y^2) = E_1 - E_2 + (F_1 - F_2 \pm |C'_2|)k_{\perp}^2$, indicating a quadratic dispersion around K , corresponding to a double Dirac point with 2π Berry phase.

C. Zeeman splitting under magnetic field

The Zeeman's coupling is obtained as,

$$H^Z(\vec{B}) = \mu_B \begin{pmatrix} g_{\parallel}^{\frac{3}{2}}B_z & & & \dagger \\ ig'_\perp B_- & -g_{\parallel}^{\frac{1}{2}}B_z & & \\ g''_\perp B_+ & g_{\perp}^{\frac{1}{2}}B_- & g_{\parallel}^{\frac{1}{2}}B_z & \\ 0 & g''_\perp B_+ & ig'_\perp B_- & -g_{\parallel}^{\frac{3}{2}}B_z \end{pmatrix}, \quad (12)$$

where $B_{\pm} = B_x \pm iB_y$ and $\mu_B = \frac{e\hbar}{2m_e}$ is Bohr magneton. Under in-plane magnetic field (which keeps TC_{2z}), the double Dirac point splits into two Dirac points with identical Berry phase π , as shown in Fig. 3(a,b). Then we consider the external magnetic field in the z direction (breaking TC_{2z}). This Zeeman field will open an energy gap at both K points, giving rise to a Chern insulator with $C = 2$.

D. Three-orbital tight-binding model

To capture the Dirac points at K points, the elementary band representations have to be $\{A_1@1a$ and $E_1@1a\}$ in the absence of SOC. Thus we choose d_{xz}, d_{yz}, d_{z^2} orbitals of Fe atoms to build the tight-binding model. The state $|d_{\alpha}, (00)\rangle$ defines the orbital d_{α} in the unit cell (mn) with respect to lattice vectors (lattice constant a), as shown in Fig. S2. Only the nearest neighbor hoppings are considered.

Consider the spin degree of freedom, the 6×6 tight-binding (tb) Hamiltonian is given below,

$$H_{tb} = \sigma_0 \otimes H(\vec{k}) + H_{so}(\vec{k}), \quad H_{so}(\vec{k}) = \begin{pmatrix} \Lambda_0(\vec{k}) & \Lambda_1(\vec{k}) \\ -\Lambda_1^T(-\vec{k}) & \Lambda_0^T(-\vec{k}) \end{pmatrix} \quad (13)$$

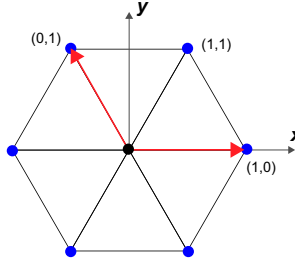


FIG. S2. Lattice of the tight-binding model with a lattice constant a . The 1a Wyckoff site is $(0,0)$ with respect to the lattice vectors, denoted by two red-colored arrows.

The $H(\vec{k})$, $\Lambda_0(\vec{k})$, $\Lambda_1(\vec{k})$ are 3×3 matrices with \vec{k} given in units of $1/a$. The up-triangle elements of the Hermitian matrix $H(\vec{k})$ without SOC are given as follows,

$$\begin{aligned}
 H_{11}(\vec{k}) &= \epsilon_1 + 2t_1 \cos k_x + (t_1 + 3t_2) \cos \frac{k_x}{2} \cos \frac{\sqrt{3}}{2} k_y \\
 H_{22}(\vec{k}) &= \epsilon_1 + 2t_2 \cos k_x + (3t_1 + t_2) \cos \frac{k_x}{2} \cos \frac{\sqrt{3}}{2} k_y \\
 H_{33}(\vec{k}) &= \epsilon_2 + 2t_3 [\cos k_x + \cos(\frac{k_x}{2} + \frac{\sqrt{3}}{2} k_y) + \cos(-\frac{k_x}{2} + \frac{\sqrt{3}}{2} k_y)] \\
 H_{12}(\vec{k}) &= \sqrt{3}(t_2 - t_1) \sin \frac{k_x}{2} \sin \frac{\sqrt{3}}{2} k_y \\
 H_{13}(\vec{k}) &= it_4 [2 \sin k_x + \sin(\frac{k_x}{2} + \frac{\sqrt{3}}{2} k_y) - \sin(-\frac{k_x}{2} + \frac{\sqrt{3}}{2} k_y)] \\
 H_{23}(\vec{k}) &= i\sqrt{3}t_4 [\sin(\frac{k_x}{2} + \frac{\sqrt{3}}{2} k_y) + \sin(-\frac{k_x}{2} + \frac{\sqrt{3}}{2} k_y)]
 \end{aligned} \tag{14}$$

with $\epsilon_1 = \langle d_{xz}, (00) | H | d_{xz}, (00) \rangle$, $\epsilon_2 = \langle d_{z^2}, (00) | H | d_{z^2}, (00) \rangle$, $t_1 = \langle d_{xz}, (00) | H | d_{xz}, (10) \rangle$, $t_2 = \langle d_{yz}, (00) | H | d_{yz}, (10) \rangle$, $t_3 = \langle d_{z^2}, (00) | H | d_{z^2}, (10) \rangle$, $t_4 = \langle d_{xz}, (00) | H | d_{z^2}, (10) \rangle$.

The spin-orbit coupling terms of $\Lambda_0(\vec{k})$ and $\Lambda_1(\vec{k})$ are derived as,

$$\begin{aligned}
 \Lambda_0(\vec{k}) &= \begin{pmatrix} 0 & i\lambda_0 & 0 \\ -i\lambda_0 & 0 & 0 \\ 0 & 0 & 0 \end{pmatrix}, \quad \Lambda_1(\vec{k}) = \begin{pmatrix} a(\vec{k}) & c(\vec{k}) & 0 \\ c(\vec{k}) & b(\vec{k}) & 0 \\ 0 & 0 & 0 \end{pmatrix}, \\
 a(\vec{k}) &= 2i\lambda_1 \sin k_x + 2ie^{-i\frac{\pi}{3}} (\frac{\lambda_1}{4} + \frac{3\lambda_2}{4}) [\sin(\frac{k_x}{2} + \frac{\sqrt{3}k_y}{2}) + e^{-i\frac{\pi}{3}} \sin(-\frac{k_x}{2} + \frac{\sqrt{3}k_y}{2})] \\
 b(\vec{k}) &= 2i\lambda_2 \sin k_x + 2ie^{-i\frac{\pi}{3}} (\frac{3\lambda_1}{4} + \frac{\lambda_2}{4}) [\sin(\frac{k_x}{2} + \frac{\sqrt{3}k_y}{2}) + e^{-i\frac{\pi}{3}} \sin(-\frac{k_x}{2} + \frac{\sqrt{3}k_y}{2})] \\
 c(\vec{k}) &= i\frac{\sqrt{3}}{2} (\lambda_1 - \lambda_2) [e^{-i\frac{\pi}{3}} \sin(\frac{k_x}{2} + \frac{\sqrt{3}k_y}{2}) + e^{i\frac{\pi}{3}} \sin(-\frac{k_x}{2} + \frac{\sqrt{3}k_y}{2})]
 \end{aligned} \tag{15}$$

with $i\lambda_0 = \langle d_{xz\uparrow}, (00) | H | d_{yz\uparrow}, (00) \rangle$, $\lambda_1 = \langle d_{xz\uparrow}, (00) | H | d_{xz\downarrow}, (10) \rangle$, $\lambda_2 = \langle d_{yz\uparrow}, (00) | H | d_{yz\downarrow}, (10) \rangle$.

TABLE S1. The parameters in the tight-binding Hamiltonian are real and given in units of eV.

ϵ_1	ϵ_2	t_1	t_2	t_3	t_4	λ_1	λ_2	λ_0
-0.5036	0.5864	-0.475	0.1434	0.4689	-0.3500	-0.0290	-0.0100	0.008

By fitting the energy bands of the DFT calculation without SOC, the parameters of $\epsilon_1, \epsilon_2, t_1, t_2, t_3$ and t_4 are obtained. The three parameters $\lambda_{0,1,2}$ are obtained by fitting the DFT bands with SOC. These parameters are listed in Table S1, and the corresponding band structures are shown in Fig. S3.

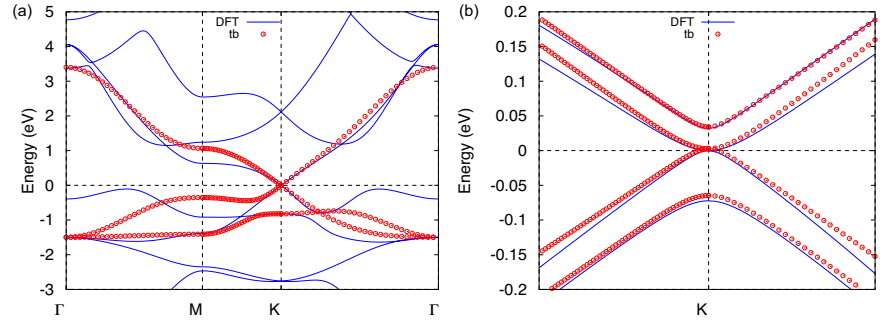


FIG. S3. The comparison between the DFT bands and the energy bands of the tight-binding model without (a) and with (b) SOC. The parameters are given in Table S1.